

Creation of Hot Radiation Environments in Laser-Driven Targets

D. E. Hinkel, M. B. Schneider, B. K. Young, A. B. Langdon, E. A. Williams, M. D. Rosen, and L. J. Suter

Lawrence Livermore National Laboratory, P.O. Box 808, Livermore, California 94550, USA

(Received 12 January 2006; published 15 May 2006)

A hot radiation environment, produced by maximizing laser-energy deposition into a small, high-Z “can,” is a platform being developed for investigations of material properties under extreme conditions. In such small targets, almost doubling the laser energy results in only an incremental increase in the x-radiation flux, and almost no increase in the maximum achieved radiation temperature. That most of this additional laser energy is not deposited within the target is a direct consequence of laser-plasma interactions (LPI) *outside* of the target, which result in high-angle beams never entering the target late in the laser pulse. Accounting for these processes in the modeling results in quantitative agreement *for the first time* with experiments using very small cans. These findings have provided the scientific foundation for modifying the target geometry to mitigate the LPI and to achieve higher radiation temperatures.

DOI: 10.1103/PhysRevLett.96.195001

PACS numbers: 52.57.-z, 52.35.Mw, 52.38.-r, 52.50.Jm

The next generation of high-energy, high-power lasers, such as the National Ignition Facility (NIF) [1] at Lawrence Livermore National Laboratory and the Laser MegaJoule [2] in France, will access a new regime of high-energy density science. Experiments on these facilities will include investigations of material properties under extreme conditions. In preparation for such studies, hot environments, where small, indirectly driven laser targets reach a high radiation temperature, are currently under development at the Omega laser [3].

A hot environment is generated when all available laser energy is deposited into a small, high-Z “can” (cf. Fig. 1). The laser beams, incident upon the inside walls of the can, excite, heat and ionize wall material. Most of the laser energy absorbed by the walls is reradiated, filling the can with x radiation, providing a radiation source.

However, these small cans also fill with ablated wall on the time scale of the laser pulse. This ablated wall material forms a plasma which absorbs laser energy before the laser beams reach the wall, thereby limiting energy deposition. In fact, in these small targets, the radiation temperature only marginally increases when the incident laser energy is doubled, a mystery explained by this work. Further, the laser spot size must be smaller than the can opening, which results in high laser intensities. Plasma filling at high laser intensity places these targets in a region of parameter space where laser-plasma interaction (LPI) is still a novel research topic.

When laser beams strike the inside of a target at normal incidence (i.e., hit the back wall) such as with targets utilized during the NIF Early Light campaign [4], models agree with measured radiation temperatures for cans with a diameter of 600 μm or larger. However, when beams are obliquely incident (i.e., hit the side walls), models agree only with measurements for cans with a diameter of 1000 μm or larger [5]. Here we demonstrate agreement for laser beams obliquely propagating into cans with a 400 μm diameter (cf. Fig. 1).

Radiation-hydrodynamics simulations using Lasnex [6] show evidence of significant plasma *outside* of small cans (those with a diameter of 800 μm or less). A laser beam propagating through this plasma creates density depressions with the ponderomotive pressure of its hot spots. If its propagation is oblique, these density depressions are swept downstream by transverse plasma flow, and a beam hot spot is refracted into the density depression it created, thereby deflecting [7]. The hot spots of the beam then self-focus and filament [8] about this new centroid. A high-angle beam (cf. 58°–62° beams in Fig. 1) may never deposit its energy inside the can. Rather, it may deflect, spray, and travel nearly parallel to the target opening, resulting in laser energy being absorbed away from the target’s field of view and hence lost.

This problem is further exacerbated by crossed-beam energy transfer (CBET) [9]. Here, pairs of beams, propagating at different angles into the can, typically overlap near the target entrance, where their intensities are high.

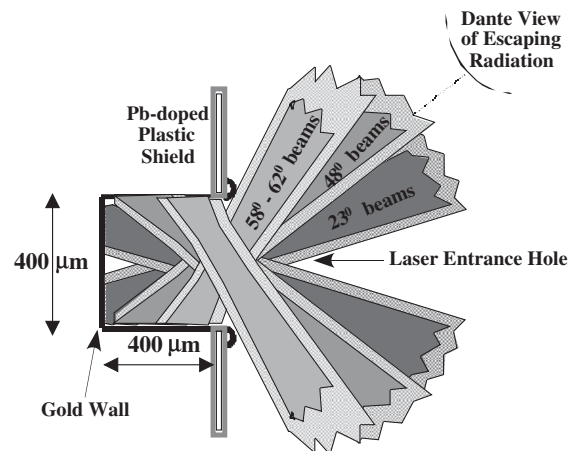


FIG. 1. Experimental setup at the Omega laser. Five laser beams enter the can at 23°, six at 48°, and nine at 58°–62°, each with 0.5 kJ of laser energy at 351 nm. X radiation leaving the can is collected at 42° relative to the target axis.

Such a pair of beams beat together to create an ion acoustic wave, and laser-energy Brillouin scatters from one beam to the other [10]. In laser-driven targets, where plasma is flowing out of the laser entrance hole (LEH), energy is transferred from a shallow-angle beam (relative to the target axis) to a beam at a steeper angle of incidence. This results in an even greater reduction in laser-target coupling, as this transferred energy may then be deflected, sprayed, and absorbed outside of the target.

In this Letter, we present evidence of LPI acting to reduce the laser-target coupling of the high-angle beams. In cans with a 400 μm diameter (also the size of the LEH), we demonstrate, for the first time, agreement between modeling and experiment when we account for such time-dependent mechanisms in modeling. When the high-angle beams, which contain almost half of the laser energy, are turned off, not only do modeling and experiments agree without invoking LPI losses, but the radiation temperature of this target is nearly identical to that in experiments with all of the high-angle beams.

For the experimental setup of Fig. 1, 20 beams at the Omega laser propagate into a can, five at 23° (inner beams), six at 48° (center beams), and nine at 58° – 62° (outer beams). The 9.5 kJ laser pulse is 1 ns in duration.

Radiation flux exiting the LEH is collected at 42° from the target axis by Dante [11], an absolutely calibrated, time-dependent x-ray spectrometer. Dante is comprised of three mirror + filter + x-ray diode and six filter + x-ray diode channels to measure x-ray energies from 0.1 to 2 keV. A separate channel measures x-ray energy in the *M*-band region of gold, 2–5 keV. The radiation temperature, T_R , is deduced from the spectrally integrated flux, ϕ_{Dante} ,

$$\phi_{\text{Dante}} = \sigma A_{\text{LEH}} \cos(42^\circ) T_R^4 / \pi, \quad (1)$$

where σ is the Stefan-Boltzmann constant, and $A_{\text{LEH}} \equiv \pi r^2$ is the area of the can opening (LEH) with radius r .

The loss of laser-target coupling in these cans is highlighted with a simple calculation. With 9.5 kJ of incident laser energy, the radiation flux from a 400 μm diameter can is typically $\phi_{\text{Dante}} \sim 640 \pm 100$ GW/sr, or $T_R = 380 \pm 15$ eV.

The radiation flux, P_R , is either absorbed in the wall or lost out the LEH, a power balance given by

$$P_R = \sigma A_W (1 - \alpha) T_R^4 + \sigma A_{\text{LEH}} T_R^4, \quad (2)$$

with $A_W = \pi r^2 + 2\pi rL$ the wall area, L the can length, and $\alpha \equiv 1 - F/(\sigma T_R^4)$ the albedo, or ratio of reflected to incident radiation flux at the wall. The quantity F in the albedo is the absorbed flux in the Marshak wave [12]. Moreover, $P_R = \eta_x \eta_a P_L$, where P_L is the input laser power, $\eta_a \sim 0.9$ the absorption efficiency, and $\eta_x \sim 0.8$ the x-ray conversion efficiency. The value of η_a is based upon backscatter measurements ($\leq 10\%$) in these targets. With these values, when we substitute (1) into (2) with $L =$

r (as holds for these targets), we find

$$P_L = \frac{1}{\eta_x \eta_a} \frac{\pi}{\cos(42^\circ)} [1 + 3(1 - \alpha)] \phi_{\text{Dante}}, \quad (3)$$

where, with $F = 0.34/(\sigma T_R^{0.66} t^{0.41})$, appropriate [13] for constant T_R (as per Fig. 5 below), $\alpha = 0.86$. The measured radiation flux is thus consistent with 5.33 TW of input laser power at 1 ns. Thus, we can account for just 56% of the 9.5 TW of actual input power at $t = 1$ ns. That is, Dante should have measured $640/0.56 \sim 1140$ GW/sr instead of 640 GW/sr.

The impact of filamentation, deflection, and CBET outside the target is demonstrated as follows. After 350 ps, in a Lasnex simulation of a 400 μm target with 9.5 TW of laser power in a 1 ns “square” pulse, the plasma has filamentation growth large enough to cause beam breakup, as well as sonic transverse flow outside of the target, which results in deflection and CBET. We extract plasma electron density, temperature, and flow conditions at this time through which we propagate two unsmoothed Omega beams (an outer and a center beam) using pF3D [14], a three-dimensional (3D), massively parallel, laser-plasma interaction code that solves the coupled paraxial light wave, electron density, and temperature equations in the fluid limit.

Figure 2, a cross section of the 3D laser intensity pattern after 18 ps of propagation, highlights relevant LPI features. Here, the dashed white line represents the LEH (all 400 μm). The abscissa is a cross section in x (in units of wavelength $\lambda \equiv 0.351$ μm for frequency-tripled 1 μm light), and the ordinate is the initial direction of propaga-

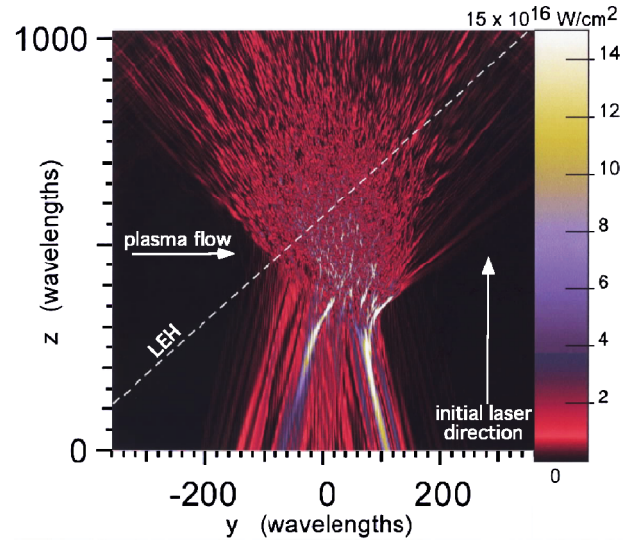


FIG. 2 (color). A cross section of a pF3D simulation of two Omega beams after 18 ps of propagation through plasma representing conditions 350 ps into the laser pulse. The initial propagation direction is along z , in units of wavelength $\lambda \equiv 0.351$ μm . The dashed line across the beam depicts the full extent of the LEH. Deflection, spray, and CBET occur outside the target.

tion into the target (also in units of λ). The plasma flow across the beam is from left to right, and is nearly shear with a Mach 1 surface about $100 \mu\text{m}$ outside of the target opening. The bending of the beam to the right is the effect of beam deflection by transverse flow, and the beam spray beyond 400λ ($140 \mu\text{m}$) is due to filamentation. After just 18 ps, 15% of the innermost beam power is transferred to the outer beam at $z = 350\lambda$, i.e., outside of the target. Further, at this time, only 62% of the laser beam energy crosses the LEH (dashed line). Later in time, even less laser energy enters the target.

We simulate this loss of coupling of the high-angle beams in Lasnex with a modification to the input power, shown in Fig. 3. Here, the dashed curve represents the experimental laser power, peaking at 9.5 TW between 700 and 1000 ps, with a total energy of 9.5 kJ. In these experiments, 25%, 31%, and 44% is on the inner, center, and outer beams, respectively. The solid curve depicts our input power to the simulation with a reduction in coupling of the high-angle beams, where we turn off the 62° beams at 500 ps and the 58° beams at 550 ps. This time-dependent loss of laser energy coupling to the target is caused by deflection, filamentation, and CBET outside of the target, and the remaining 5.3 TW of the incident flux is consistent with our results from Eq. (3).

Figure 4 is a plot of the Dante radiation flux versus time. The hatched black region is the experimental measurement including its uncertainty. The simulation results are represented by the solid black curve. This simulation not only agrees well in peak flux with the experimental results, but it also reproduces the temporal profile. Without LPI “losses” the simulated results are vastly discrepant: the radiation flux peaks far above the experimental results, and the

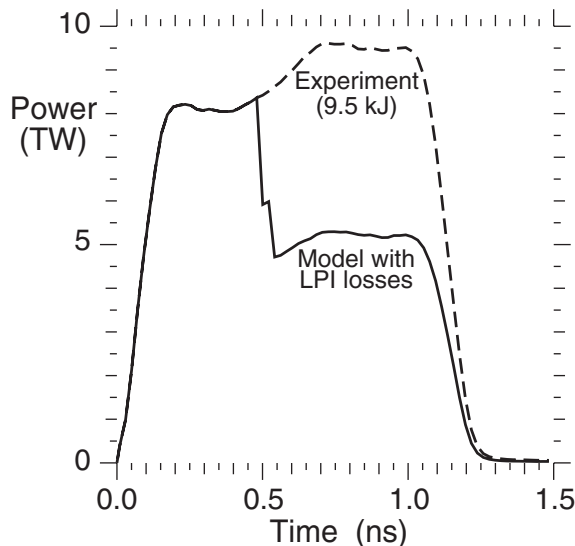


FIG. 3. Laser power versus time. The dashed curve represents the experimental profile. Simulation results where the input power is given by the solid curve account for LPI losses on the outer beams.

temporal profile is altered such that the radiation flux climbs to and peaks at ~ 1 ns.

We also shot targets without the high-angle (outer) beams, i.e., with 44% less power. These Dante results are also shown in Fig. 4, and are depicted by the shaded red region (which includes the uncertainty in measurement). The corresponding simulation results are depicted by the solid red curve. This simulation was performed using 56% of the dashed curve of Fig. 3 for the input laser power, and shows that when the high-angle beams are omitted, it is not necessary to account for any LPI losses.

There are several striking features in Fig. 4. First, the level of radiation flux collected by Dante is almost the same with and without the high-angle beams between 0.8 and 1.5 ns, which suggests that during this time these beams do not couple their energy to the target. Moreover, early in time, the high-angle beams do couple to the target, as is evidenced by the large difference between the red and black curves around 0.5 ns. Finally, the temporal shape of the two curves differ: without the high-angle beams (red curve), the radiation flux peaks right around the time that the laser beams shut off (~ 1 ns), whereas with all three beam cones and higher power (black curve), the peak radiation flux is essentially reached by 0.5 ns.

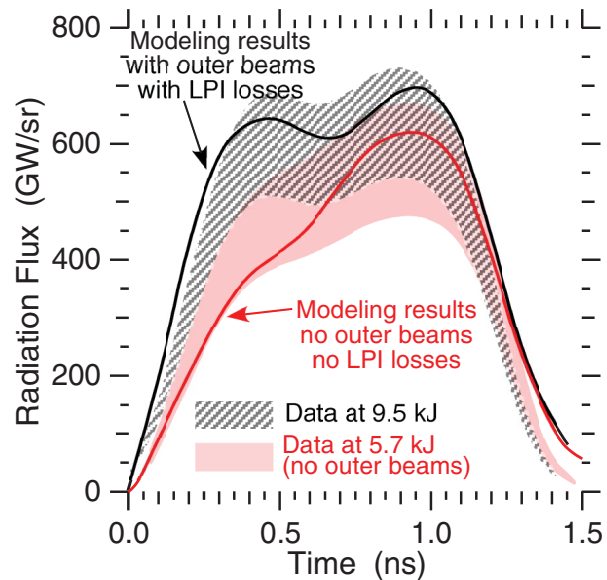


FIG. 4 (color). Radiation flux collected at 42° from the target axis. The measurement corresponding to the dashed curve of Fig. 3 is depicted by the hatched black region (including uncertainty). The solid black curve depicts the simulation results when we account for LPI losses by using the solid curve of Fig. 3 for the input power, which shows quantitative agreement with the measurement. Experimental results without the high-angle beams result in a radiation flux represented by the shaded red region. Such experiments use $\sim 56\%$ of the dashed line of Fig. 3 as input power. The solid red curve is the result from a simulation using the same input power as for the red-shaded region, i.e., without accounting for LPI losses.

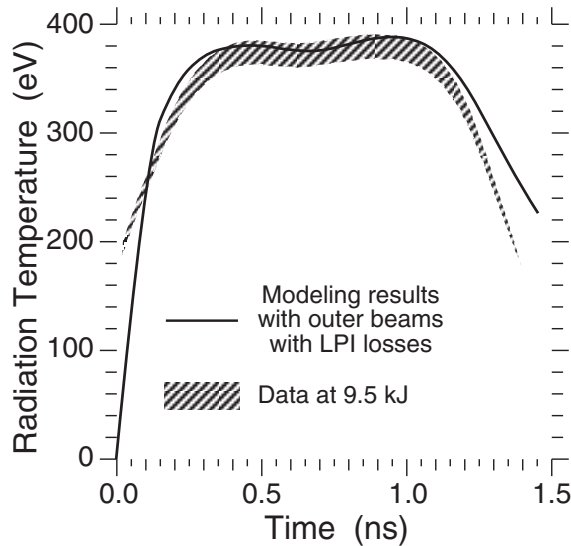


FIG. 5. Radiation temperature derived from the radiation flux using Eq. (1). The experimental results with its uncertainty are shown in gray. The simulation results are represented by the solid curve, showing good agreement with experiment. Not accounting for LPI losses in the simulation would result in disagreement between these two curves.

We calculate the input power that corresponds to the drive given by the mean value of the shaded red region around time $t = 1$ ns, or $\phi_{\text{Dante}} = 575$ GW/sr ($T_r = 370$ eV). Here, the albedo is given by its constant power form (with T_R rising) [13], or $\alpha = 1 - 0.46 / (\sigma T_r^{0.66} t^{0.54}) = 0.81$. Substitution into Eq. (3) with η_x and η_a as before yields $P_L = 5.3$ TW, a value very near the input laser power level of 5.7 TW. Thus, without the high-angle beams we account for all of the power.

The radiation temperature can be derived from the radiation flux, using Eq. (1). Figure 5 depicts the radiation temperature versus time, where the hatched black region represents the experimental measurement, including its uncertainty, when full laser power (and thus all three beam cones) as depicted by the dashed curve in Fig. 3 is used. The simulated radiation temperature, using the solid curve of Fig. 3 for the input laser power and thus accounting for LPI losses, is depicted by the solid curve.

Our findings corroborate that when the target is not driven with high-angle beams, incident energy is better coupled, and radiation-hydrodynamics simulations do not have to account for LPI losses. The shallower the angle of the beam, the larger the opening of the target as seen by the beam [$r_{\text{opening}} = r_{\text{LEH}} \cos(\theta)$, where $\theta \equiv$ the angle of incidence of beam propagation with respect to the target axis]. Also, because the beam angle is small, there is less transverse flow across the beam and hence less deflection. Filamentation outside the target still occurs, but not about a severely deflected centroid.

We plan to investigate “hyperbolic” cans, where the wall surface area is nearly the same as in a cylindrical

can but where the LEH has a larger diameter than that of the back wall. In such targets beam filamentation, deflection, absorption, and CBET outside of the entrance hole should not have as grave a consequence, because of the increased radius of the target opening as well as the modified plasma flow out of the target. Such targets hold the hope of creating even hotter environments.

In summary, there is a loss of laser-energy coupling in small, laser-driven cans when beams enter the target at a steep angle of incidence. This loss, a consequence of filamentation, deflection, absorption, and crossed-beam energy transfer outside of the target, results in less laser energy available to the target. We have demonstrated, for the first time, quantitative agreement between modeling and experiment for these small targets when we temporally account for such losses in simulations.

We acknowledge valuable input from O.L. Landen, R.L. Kauffman, R.E. Turner, K.M. Campbell, J. Schein, F.A. Weber, and the Omega team. This work was performed under the auspices of the U.S. Department of Energy by the University of California Lawrence Livermore National Laboratory under Contract No. W-7405-ENG-48.

- [1] G.H. Miller, E.I. Moses, and C.R. Wuest, Nucl. Fusion **44**, S228 (2004).
- [2] M.L. Andre, Proc. SPIE Int. Soc. Opt. Eng. **3047**, 38 (1997).
- [3] J.M. Soures *et al.*, Phys. Plasmas **3**, 2108 (1996); T.R. Boehly *et al.*, Opt. Commun. **133**, 495 (1997).
- [4] D.E. Hinkel *et al.*, Phys. Plasmas **12**, 056305 (2005); E.L. Dewald *et al.*, Phys. Rev. Lett. **95**, 215004 (2005).
- [5] E. Dattolo *et al.*, Phys. Plasmas **8**, 260 (2001).
- [6] G. Zimmerman and W.L. Kruer, Comments Plasma Phys. Control. Fusion **2**, 51 (1975).
- [7] H.A. Rose (private communication); J.D. Moody *et al.*, Phys. Rev. Lett. **77**, 1294 (1996); D.E. Hinkel, E.A. Williams, and C.H. Still, Phys. Rev. Lett. **77**, 1298 (1996).
- [8] F.W. Perkins and E.J. Valeo, Phys. Rev. Lett. **32**, 1234 (1974); W.L. Kruer, Comments Plasma Phys. Control. Fusion **9**, 63 (1985); R.L. Berger *et al.*, Phys. Fluids B **5**, 2243 (1993); P.E. Young *et al.*, Phys. Rev. Lett. **75**, 1082 (1995).
- [9] R.K. Kirkwood *et al.*, Phys. Rev. Lett. **76**, 2065 (1996); W.L. Kruer *et al.*, Phys. Plasmas **3**, 382 (1996); E.A. Williams *et al.*, Phys. Plasmas **11**, 231 (2004).
- [10] V.P. Silin, Sov. Phys. JETP **21**, 1127 (1965); J.F. Drake *et al.*, Phys. Fluids **17**, 778 (1974); D.W. Forslund, J.M. Kindel, and E.L. Lindman, Phys. Fluids **18**, 1002 (1975); W.L. Kruer, *The Physics of Laser Plasma Interactions* (Westview Press, Boulder, CO, 2003).
- [11] C. Decker *et al.*, Phys. Rev. Lett. **79**, 1491 (1997).
- [12] M.D. Rosen, Proceedings of the Scottish Universities Summer School in Physics 2005, edited by D. Jaroszynski (to be published).
- [13] J.H. Hammer and M.D. Rosen, Phys. Plasmas **10**, 1829 (2003).
- [14] C.H. Still *et al.*, Phys. Plasmas **7**, 2023 (2000).